AIAA 96-0865

Spectral Analysis and Experimental Modeling of Ice Accretion Roughness

D.J. Orr, K.S. Breuer, B.E. Torres and R.J. Hansman, Jr.
M.I.T.
Cambridge, MA

34th Aerospace Sciences Meeting & Exhibit
January 15-18, 1996 / Reno, NV

Spectral Analysis and Experimental Modeling of Ice Accretion Roughness

D. J. ORR*, K. S. BREUER†, B. E. TORRES‡ & R. J. HANSMAN, JR.§

Department of Aeronautics and Astronautics
Massachusetts Institute of Technology
Cambridge, MA 02139

Abstract

A self-consistent scheme for relating wind tunnel ice accretion roughness to the resulting enhancement of heat transfer is described. First, a spectral technique of quantitative analysis of early ice roughness images is reviewed. The image processing scheme uses a spectral estimation technique (SET) which extracts physically descriptive parameters by comparing scan lines from the experimentally-obtained accretion images to a prescribed test function. Analysis using this technique for both streamwise and spanwise directions of data from the NASA Lewis Icing Research Tunnel (IRT) are presented. An experimental technique is then presented for constructing physical roughness models suitable for wind tunnel testing that match the SET parameters extracted from the IRT images. The icing castings and modeled roughness are tested for enhancement of boundary layer heat transfer using infrared techniques in a "dry" wind tunnel.

1 Introduction

Quantitative characterization of early-stage surface roughness is a key aspect of modeling glaze ice growths since it is the initial roughness that establishes the convective heat-transfer coefficient and subsequently determines the freeze-out of excess surface water under glaze conditions[8]. Consequently, early stage roughness provides a mechanism for the formation of more ice, raising the prospect of correlating long term ice shapes to the initial roughness characteristic of the corresponding cloud conditions. In addition, surface roughness also plays a pivotal role in triggering the laminar-turbulent transition of the boundary layer, resulting in a substantial increase in convective heat transfer. State-of-the-art ice accretion codes such as NASA's LEWICE represent the enhanced heat transfer that results from surface roughness with the Equivalent Sand Grain Roughness (ESGR) model[6]. Thus, the substantial complexity of early glaze accretions is reduced to a single ESGR parameter, k, upon which heat transfer correlations are based. The limitations of the ESGR correlations are particularly evident when one recalls that their original definition was only to establish a uniform standard for correlating the pressure drop along a pipe with a rough surface and has no relation to heat transfer, let alone multi-phase ice accretions[5]. ESGR is often used in current icing codes as a free parameter that is adjusted until the simulated ice shape matches a given experimentally observed ice shape. It is apparent that this description of roughness is problematic when one realizes that the value of k required to create realistic ice shapes often bears no relation to the roughness scales observed in the real accretion. Consequently, a priori determination of glaze ice shapes is difficult. The role of the ESGR parameter k as an input quantity to LEWICE is depicted in Figure 1. The goal of this work is to provide an alternative to the ESGR heat transfer correlations based upon interpretation of close-up images detailing ice accretion micro-physics. This will be accomplished by applying image processing techniques to obtain a quantitative description of key accretion features and then constructing simulated roughness for use in "dry" heat transfer experiments. The results of these experiments can potentially provide a basis for more sophisticated heat transfer correlations for use in computer icing codes. A schematic of the proposed heat transfer model and its relationship to LEWICE is given in Figure 1.

*Research Assistant
†Assistant Professor, Member AIAA
‡Research Assistant
§Professor, Associate Fellow AIAA

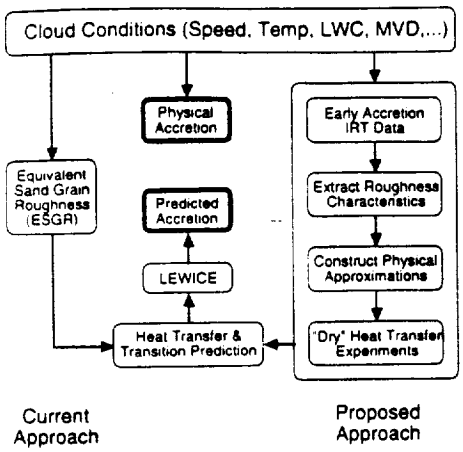

Figure 1: Schematic of current and proposed heat transfer model in LEWICE.

NASA IRT experiments[3] have provided high magnification video images which represent a continuous record of developing ice accretions that spans from the first seconds of ice formation until the long term ice shape has been established approximately 10 minutes later. Consequently, quantitative analysis of such data requires techniques which fall under the rubric of image processing. Recent work[6] in modeling early stage roughness in ice accretions has led to two schemes for quantitative analysis of high resolution video images obtained from NASA Lewis IRT experiments. These methods provide an alternative to the Equivalent Sand Grain Roughness (ESGR) model which may produce non-physical roughness scales when used for enhanced heat transfer correlations in ice accretion codes such as LEWICE.

The first of these methods is a structural-stochastic model based upon the theory of Markov random field texture modeling[1]. This technique is capable of producing realistic looking roughness but is difficult to interpret physically[6]. The second scheme is the Spectral Estimation Technique (SET) which describes ice accretion images by a characteristic ice "bead" size and spacing. While this characterization represents a considerable simplification of extremely complicated images, the bead-spacing model mimics the localized growths of ice that dominate early formation of glaze ice accretions.

Masiulaniec et al.[4] developed a technique for making investment castings of actual ice shapes from IRT experiments. By providing a direct reproduction of the roughness topography, such castings remove the ambiguity in interpreting uncalibrated grayscale video images. The work of Henry et al.[2] utilizes infrared thermography to measure the enhanced heat transfer on roughness samples in dry wind tunnel experiments. This study combines the IRT video data of Hansman[3], the analysis of the SET[6], the castings of Masiulaniec[4], and the technique of Henry[2] into a self-consistent scheme which connects close-up IRT video images to enhanced heat transfer observed on "similar" artificial roughness in dry wind tunnel tests. Similarity between experimentally-observed surface roughness and artificial roughness is defined in terms of comparable SET parameters. The paper begins with an overview of available data followed by a review of the SET, the application of the SET to close-up IRT icing images and the introduction of a technique for creating images based upon experimental SET parameters. Next, a process for constructing physical roughness models suitable for heat transfer tests in a wind tunnel is demonstrated. The study concludes with the observation of enhanced heat transfer on physical roughness models in dry wind tunnel tests.

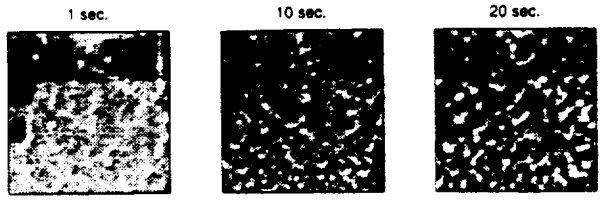

Figure 2: Time sequence of glaze accretion. Dark regions in upper portion of images are from markings on the wind tunnel model and were cropped out of data used for streamwise calculations.

2 Sample Images

2.1 NASA Lewis IRT Data

The techniques in this paper are applied to two sets of data. The first image set is the high-magnification video data taken from ice accretion experiments[3] described by Hansman et al. in which a 4" diameter cylinder (faired in the back) was exposed to the icing cloud over a wide rage of wind speeds, temperatures and liquid water content. Simultaneous video images of both the overall and the stagnation region (taken with a long-focal-length lens stationed in the IRT control room) were taken during that experiment, although only the close-up images are used in this study. Figures 2 and 3 show a typical time sequence of glaze and mixed accretions, respectively. The brightly lit areas can be

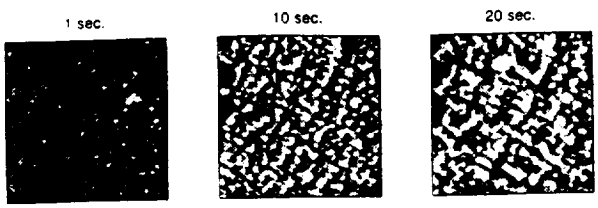

Figure 3: Time sequence of mixed accretion. Dark regions in upper portion of images are from markings on the wind tunnel model and were cropped out of data used for streamwise calculations.

interpreted as ice bumps which reflect the illuminating light while the dark areas are the valleys between roughness elements. This interpretation is rather subjective since other geometric features, such as glare from the model (which was aluminum) or reflection by surface water, might give a misleading impression of the surface texture. Nevertheless, the image is descriptive of the accretion physics although the interpretation must proceed with caution. Note the bead-like character of the mixed case in Figure 3. It is the presence of these localized ice growths in the early stages of glaze and mixed accretions that is the motivation for the bead diameter/bead spacing model of the SET. Although the ice bumps are not as clearly defined in the glaze case as they are in the mixed case, it is also apparent that there does seem to be a characteristic range of bump sizes in the glaze image.

2.2 Icing Roughness Castings

The second image set is derived from the models used in the wind tunnel heat transfer experiments of Masiulaniec et al.[4] These models consisted of castings from flat plate ice shapes taken at the NASA Lewis IRT. In the IRT experiments that produced the castings, a flat plate was exposed to an icing cloud which produced ice roughness that varied primarily with streamwise location on the plate. Once an accretion was established, the experiment was halted and a casting was made of the surface. These large castings were then partitioned into smaller sectors whose dimensions were sufficiently small so that the icing roughness was qualitatively similar within a particular sector. In Figure 4, the casting was taken at a more advanced stage in the accretion when many of the interstices between the initial ice beads had been filled with accumulations of additional ice causing some of the early bead-like structures to merge into larger roughness elements of

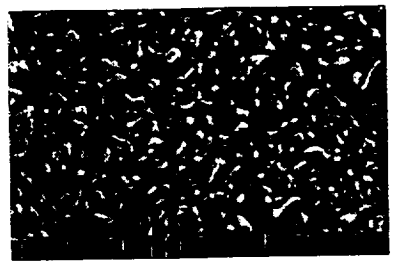

Figure 4: Surface roughness casting image from a model used in the heat transfer experiments of Masiulaniec et al. Scale on the image is in millimeters.

complex connectivity. As will be discussed in the "SET Calibration" section of this paper, the castings are not ideal for SET analysis, but provide an opportunity to conduct comparative heat transfer studies on actual ice shapes and the corresponding SET-derived artificial roughness samples. The NASA IRT video images of glaze and mixed accretions are more amenable to SET analysis but no castings exist of the roughness at early stages ($\sim$ 1 min.) since the experiments were also designed to investigate long term ($\sim$ 10 min.) ice shapes.

3 SET Review

3.1 General Concepts

Figures 2 and 3 show the localized ice growths that typify the first 20 seconds of glaze and mixed growths, respectively. The goal of the Spectral Estimation Technique (SET) is to characterize the sizes and spacings of these ice beads by minimizing the error between scan lines of image data and a fit "test function." Mathematically, one can construct a periodic test function which approximates image scan lines in the spatial domain. The test function can, in principle be arbitrary but for the present analysis, the function chosen consists of a periodic extension of sinusoidal "beads:"

$$F_{test}(x) = \begin{cases} \sin(\frac{\pi x}{D}) & \text{if } 0 \le x \le D \\ 0 & \text{if } D < x \le P \end{cases}$$

where P is the period of the test function and D is the width of the bead[6]. Thus, the SET extracts the dominant length scales (D,P) to produce a physically relevant model which serves as a basis for experimental efforts in constructing physical surface roughness suitable for wind tunnel testing. A certain degree of flexibility is achieved because the SET

yields multiple bead size/spacing pairs, allowing one to choose the most dominant combinations to model the roughness. Therefore, a "one-bead" SET model is a two parameter representation of the roughness in contrast to the one parameter representation of the ESGR. Higher order SET representations of the roughness are easily obtained by retaining additional bead size/spacing pairs.

Although we have fit only the bead width and spacing, other shape parameters, such as "roundness," symmetry, etc. could also be included without any difficulty although the computational resources required for the optimization will necessarily increase. As described, the test function is used to model only horizontal (streamwise) scan lines in the images. It is expected that the bead geometry will be different in the streamwise and spanwise directions and for this reason one should ideally employ a two-dimensional test function and optimize for the roughness characteristics in both the spanwise and streamwise directions on the model surface. This extension, which would utilize the full two-dimensional power spectrum, is not difficult but was not used in the current study in order to simplify the initial investigation and to reduce the parameter space for the optimization procedure. The analysis in the span direction consisted of the same one-dimensional scheme that was used for the streamwise direction.

3.2 SET Algorithm

With the test function defined, the procedure for optimizing D and P is as follows:

1. The power spectrum (Q) for discrete wavelengths (λ) of a single horizontal scan line of experimental data was computed using Fast Fourier Transform (FFT) techniques ($Q(\lambda)_{expt}$).

2. Once a $D-P$ combination was selected, the corresponding test function and its power spectrum was computed ($Q(\lambda)_{test}$).

3. Because the IRT video data were not calibrated for amplitude, the spectrum of the test function was normalized so that maxima of the two spectra were equal. This removed any bias due to uneven lighting or amplitude effects.

4. The "error" in the estimation was computed from the sum of the difference between the experimental and test spectra at each wavelength: $error = \sum_{\lambda=\lambda_{min}}^{\lambda_{max}} |Q(\lambda)_{expt} - Q(\lambda)_{test}|$ where λ_{min} and λ_{max} represent the minimum and maximum wavelengths to be considered (typically 0.03 and $5mm$, respectively).

5. The optimal $D-P$ combination was determined by minimizing the absolute error over all physically reasonable combinations of D and P.

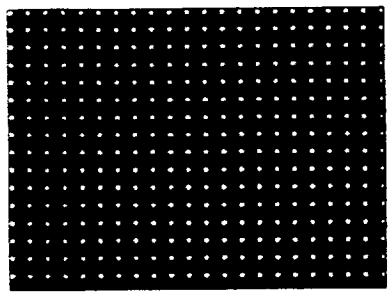

Figure 5: Rectangular Bead Array: D = 10 pixels, P = 30 pixels (480 x 640 pixels)

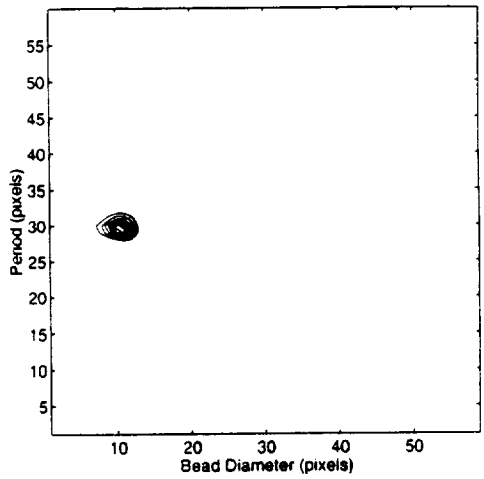

Figure 6: Horizontal SET Histogram for Figure 5

For an image of n scan lines, application of the SET algorithm produces n (D,P) combinations. This set of n ordered pairs is then presented as a two-dimensional joint histogram over the $D-P$ domain considered.

It should be noted that due to the simplicity of the test function, analytical expressions for the test function power spectrum may be used to expedite the calculations.

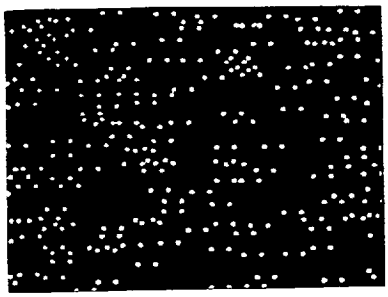

Figure 7: Pseudo-random Bead Array: $D = 10$ pixels, $P = 30$ pixels (480 x 640 pixels). Same bead density as rectangular bead array in Figure 5

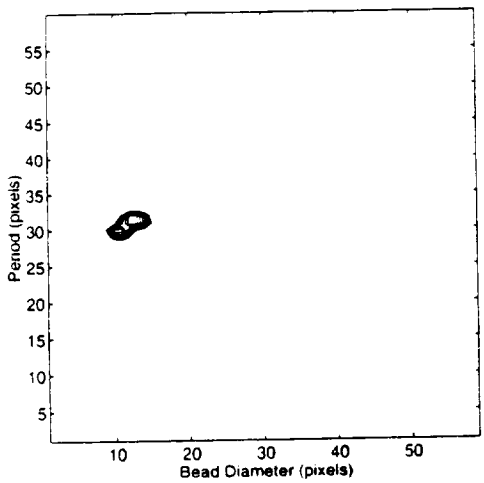

Figure 8: Horizontal SET Histogram for Figure 7

3.3 Validation of the SET

3.3.1 Rectangular Bead Arrays

As test cases for the SET algorithm, idealized images containing known bead diameter and bead spacing length scales were analyzed. The SET results were then checked to see that the optimal test function parameters were indeed the prescribed length scales. Figure 5 shows a rectangular matrix of beads and Figure 6 depicts the corresponding horizontal SET histogram for fixed diameter $D = 10$ and period $P = 30$. As can be seen, the corresponding two-dimensional SET histogram has a strong peak at approximately $(D, P) = (10, 30)$. Some smearing of the peak is to be expected since a given scan line will not, in general, pass exactly through the center of a row of beads. Additional uncertainty arises from the fact that the image beads are not identical in mathematical form to the SET test function.

When two greatly disparate bead sizes are present, the SET tends to emphasize the larger bead sizes. This is because the larger beads contain more spectral power and consequently are approximated most effectively by test functions with large bead diameters. While it is possible to create test cases in which the small bead sizes are ignored in favor of relatively large beads, one can usually detect smaller bead sizes by the presence of secondary peaks in the joint (D, P) SET histogram. It is possible that the interference of large beads in the detection of smaller beads could be eliminated using a multiple-scale analysis. For example, a multiple-scale scheme might involve sophisticated techniques such as wavelet filtering or a proper orthogonal decomposition to separate the ice features according to size in a pre-processing step before application of the SET. However, after preliminary study, it is not clear that the cost of adding this level of complexity to the SET would be worth the benefit realized since the larger beads offer a reasonable first approximation to the roughness and may even dominate the heat transfer enhancement in the icing problem.

3.3.2 Pseudo-random Arrays

Test images more representative of physical ice accretions may be produced by depositing beads of specified diameter and inter-bead spacing in pairs at arbitrary locations in the image until a target bead density is achieved. Figure 7 depicts a pseudo-random array with the same bead density as Figure 5 for $(D, P) = (10, 30)pixels$. Figure 8 depicts the corresponding SET histogram for the horizontal scan lines. The SET histogram reveals a peak at the expected location of $(D, P) \approx (10, 30)pixels$. If SET parameters are to be specified in both the horizontal and vertical directions within a single image, the test beads can be deposited in triplets with different inter-bead spacings in either direction. The underlying motivation for this image generation technique is the desire to measure the horizontal and vertical SET parameters from a given experimental image, compute a two-dimensional bead density from a rectangular bead array possessing these parameters, and then produce a pseudo-random bead array with SET parameters similar to the original image. The image generation technique presented above uses a somewhat limited two-dimensional test function in the sense that the roughness element diameters in both the horizontal and vertical directions are assumed to be comparable. That is, this model would apply to images that were composed primarily of

bead-like elements rather than structures that were elongated in a particular direction. This assumption is more likely to be valid for early stage icing roughness which is typically composed of localized ice growths. The ice growths increase in density and merge at longer accretion times to form complicated, interconnected patterns. In light of this, one might expect the bead model to more accurately characterize the early IRT video images which were taken during the first 20 seconds of exposure to cloud conditions rather than the casting images which resulted from exposure times an order of magnitude greater. In fact, the SET histograms for the IRT video data do contain much less noise than their casting image counterparts (see Figures 9, 10 and Figures 11, 12), implying that the test function was a better "fit" for the IRT images. Also, qualitative comparison of the IRT and casting images shows that while there does seem to be characteristic length scales present in both images, the casting is significantly more complicated and possesses interconnected elements that deviate from idealized bead-like roughness due to the more advanced stage in the accretion when the casting was taken. This suggests that the bead model is more appropriate for the early stage roughness. However, this is not really a limitation since, as previously discussed, it is the role of early stage roughness in enhancement of heat transfer and boundary layer transition that is primarily of interest.

4 Application of the SET to Experimental Data

The SET histograms for the streamwise (horizontal) and spanwise (vertical) directions for the second frame of the mixed accretion in Figure 3 are given in Figures 9 and 10. The two highest peaks in the horizontal histogram are at $(D, P) \approx (0.5, 0.83)mm$ and $(D, P) \approx (0.63, 1.06)mm$. For the vertical histogram given in Figure 10 the two highest peaks are at (D, P) pairs of $(0.47, 0.77)mm$ and $(0.57, 1.16)mm$ although it is noted that other comparable peaks exist. This suggests a certain degree of isotropy in the accretion image. Qualitative inspection of the grayscale image reveals that while it may be difficult to estimate interbead spacings, the roughness elements do appear to have approximately the same dimensions in both the stream and span directions, lending credence to claims of isotropic roughness. This is reasonable since the image was taken only 10 seconds into the accretion and round roughness elements do not start to become distorted until mechanisms such as streamwise rivulets of surface water dominate at longer times. The SET histograms for the streamwise and spanwise directions for the roughness casting of Figure 4 are given in Figures 11 and 12. There are two dominant structures in the spanwise SET histogram at (D, P) combinations of $(0.93, 1.79)mm$ and $(0.79, 3.57)mm$. Consideration of the streamwise SET histogram reveals a dominant peak at $(1.14, 3.93)mm$. Numerically, the second largest structure is at $(0.89, 1.68)mm$ although the presence of the peak is not as clear as its counterpart in the spanwise SET histogram at $(0.93, 1.79)$. As noted earlier, there is clearly more noise in the SET histograms of the casting image than in the early accretion images of the IRT data due to the

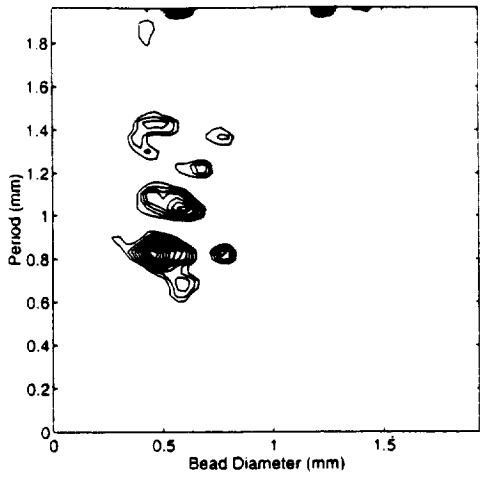

Figure 9: SET histograms for second frame of Figure 3: streamwise (horizontal) SET

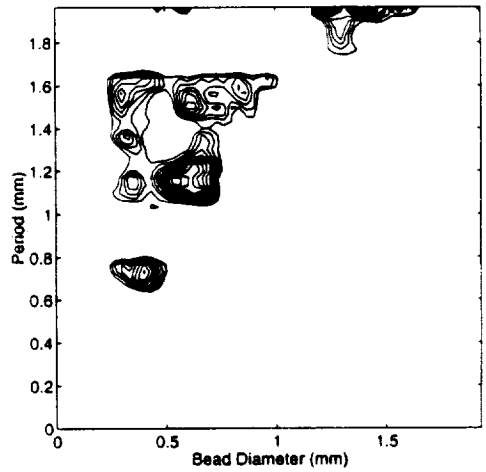

Figure 10: SET histograms for second frame of Figure 3: spanwise (vertical) SET

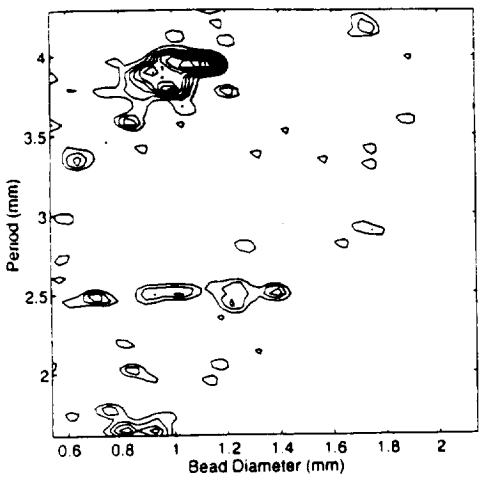

Figure 11: SET histogram for casting image of Figure 4: streamwise (vertical) SET

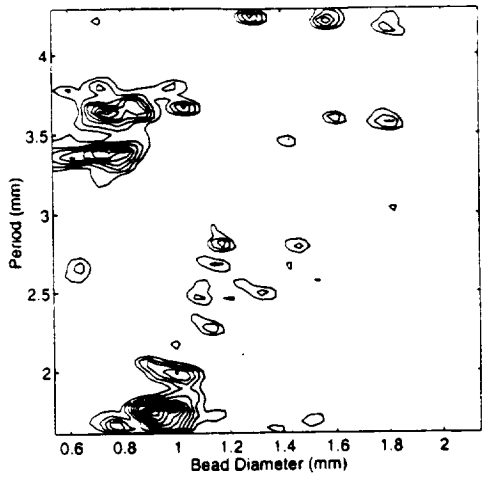

Figure 12: SET histogram for casting image of Figure 4: spanwise (horizontal) SET

more bead-like nature of early stage roughness.

5 Simulated Roughness for Dry Wind Tunnel Testing

One of the strengths of the SET is that the parameters produced by the method have clear physical interpretations. This is an important aspect of the analysis since such a scheme is easily translated into a production technique for physical roughness models. In the language of image processing, the SET is a primitive object placement rule technique. This simply means that simulated textures are composed of well-defined primitive objects at possibly different scalings which are inserted into a texture field according to some placement rule. For the SET, the primitive objects are beads and the placement rule is composed of bead spacing selection, bead overlap prohibition, and a bead number density criterion. In contrast, stochastic texture analysis techniques which utilize parameters such as fractal dimension and Markov random field annealing constants[7] do not always have clear physical meaning in the context of physical roughness production. Consequently, the efficacy of these characterizations of icing roughness as a guide to experimental roughness construction is questionable. Alternatively, the obvious extension of the SET to a construction scheme for physical roughness samples is an automated bead deposition technique. One such scheme is described below.

5.1 Hardware

The technique for constructing physical roughness samples is epoxy bead deposition using an automated syringe. The apparatus used to deposit epoxy beads (Figure 13) consists of a three-dimensional computer-controlled traverse which positions a precision micro-liter syringe for delivery of a soft, slightly thixotropic two-part epoxy. The traverse positions the syringe to an accuracy of $0.007mm$ in three dimensions over a substrate area of $28cm$ x $28cm$. A fourth computer-controlled axis actuates the plunger on the syringe to dispense set volumes of epoxy. The epoxy selected provided a working time in excess of 2 hours and was of thin consistency but could be thickened by pre-curing to provide larger contact angles between the droplet and the substrate. The needle sizes used ranged between 26 gage and 18 gage which produced droplet sizes from $0.4mm$ to over $2mm$. This range of bead sizes was consistent with the length scales observed in the IRT video images as well as the casting images. Blunt, 90° bevel needles were used so that the epoxy on the tip of the needle could be touched to the substrate and the bead inflated to the desired volume. This prevented excess epoxy from clinging to the needle tip and resulting in irregular bead volumes on successive applications. The substrates used were polished aluminum and Plexiglas. In order to provide reasonable bead contact angles, the substrates were treated with wax or a combination of wax and paint. To control the bead heights, one could control the volume of epoxy delivered, thicken the epoxy with pre-curing, or "build up" individ-

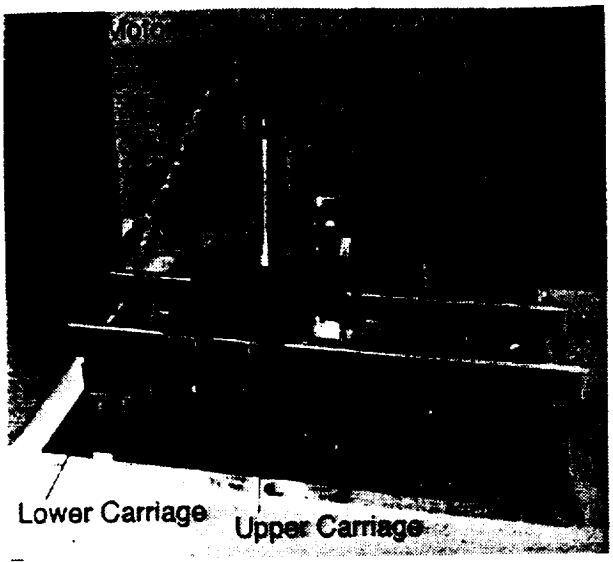

Figure 13: Three-dimensional traverse for automated epoxy bead deposition. X, Y and Z axes control syringe position while W axis controls the syringe plunger.

ual beads with multiple applications of epoxy between partial curings. Additional techniques useful for control of bead geometry include adjustment of the substrate temperature and curing the bead arrays upsidedown to prevent flattening of the beads under the influence of gravity. For a bead diameter of $2mm$, obtainable bead heights ranged from $0.2mm$ to $0.75mm$.

5.2 Syringe Calibration with the SET

To calibrate the syringe/epoxy assembly, an array of test beads was deposited for different syringe plunger displacements. This calibration array is shown in Figure 14. The SET was then used to analyze the various scan lines for each bead size in the calibration image. Bead diameters from the SET histograms for each plunger displacement were noted and plotted (Figure 15). Since the plunger displacement is proportional to volume of epoxy delivered which is in turn proportional to the bead diameter cubed, it is not surprising that data of Figure 15 are well fit by a curve with a cube root dependence on syringe plunger displacement. It should be noted that if factors such as the needle size, epoxy consistency, or substrate treatment is altered, a new calibration curve must be constructed.

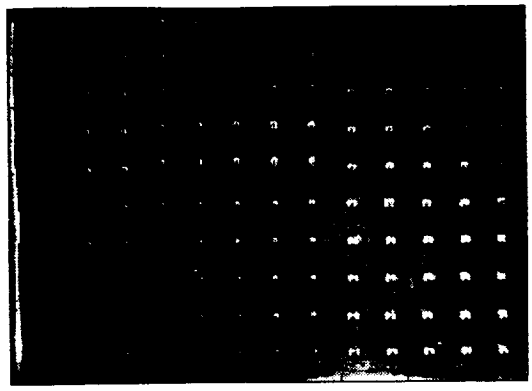

Figure 14: Epoxy bead array for SET-based calibration of syringe. Horizontal field of view is $7cm$. Various syringe plunger displacements are used to produce beads of different sizes ($0.4mm$ - $1.4mm$).

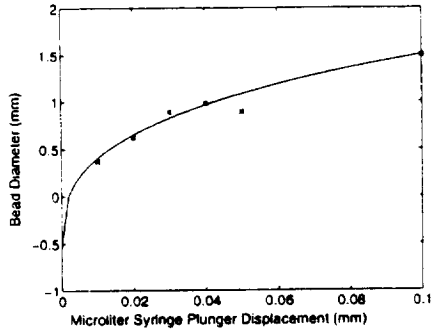

Figure 15: SET-based calibration curve for syringe/epoxy assembly.

5.3 Modeling of Casting Data

As previously mentioned, the casting images are less than ideal for SET analysis due to the long accretion times which bring into question the validity of the isolated bead array model implicit in the SET. However, the castings do provide the opportunity for wind tunnel tests that directly compare enhanced heat transfer on the SET-based roughness to enhanced heat transfer on the real icing roughness (as represented by the castings).

The first step in the process is to photograph the castings and perform the SET analysis. The casting used is that shown in Figure 4. The SET histograms for the streamwise and spanwise directions are given in Figures 11 and 12. The dominant (D, P) combination in the spanwise SET histogram at $(0.93, 1.79)mm$ and the corresponding streamwise peak at $(0.89, 1.68)mm$ were selected as a first approximation to modeling the casting roughness.

Figure 16: Experimental Epoxy Bead Arrays: Rectangular Array (17mm x 28mm)

Figure 17: Experimental Epoxy Bead Arrays: Staggered Rectangular Array (17mm x 28mm)

Figure 18: Experimental Epoxy Bead Arrays: Pseudo-Random Array (17mm x 28mm)

Next, the roughness arrays are constructed using the epoxy bead deposition technique described above. The roughness array configurations selected for this study are shown in Figures 16, 17 and 18. The bead density for the pseudo-random array was equal to that of the rectangular array. A staggered array whose adjacent rows are 180° out of phase was also investigated.

The SET analysis is then applied to photos of the epoxy bead arrays to check that the SET parameters are those prescribed by the analysis of the casting image. As the final step in correlating the modeled roughness to the experimental icing roughness, comparative heat transfer studies are conducted in a dry wind tunnel on the epoxy bead arrays and the experimentally-obtained casting.

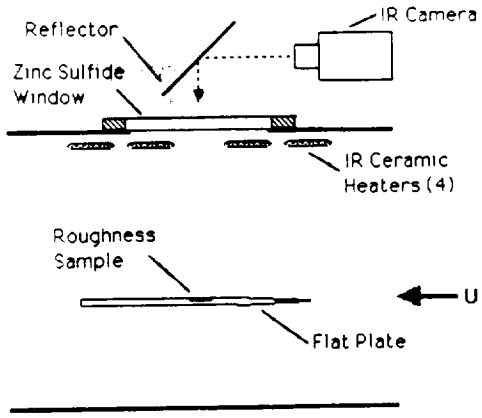

Figure 19: Experimental Setup for Dry Heat Transfer Tests

6 Dry Wind Tunnel Testing

6.1 Experimental Setup

Heat transfer tests were conducted in a low-speed, in-draft wind tunnel at the NASA Lewis Research Center. The apparatus and experimental techniques are similar to those of Henry et al.[2] The models used consisted of a flat plate with the roughness plugs of Figures 4, 16 17, and 18 installed at the mid-chord of the plate such that the substrate was flush with the plate surface. Two plugs, located at the same chordwise location but different span locations were tested during each run.

A schematic of the test section is shown in Figure 19. In addition to the roughness plugs, the plate was instrumented with 8 thermocouples (4 on the test side and 4 on the underside) and 10 static pressure ports located on the centerline. A temperature differential was established between the plate and the flow by a configuration of four 12cm x 12cm infrared (IR) ceramic heaters operating at 1000W, 225V, and an average surface temperature of 750°C. To insure uniform heating and prevent reflective heat losses, the roughness substrate was painted flat black. To minimize heat loss by conduction, both the roughness plugs and the plate were constructed of Plexiglas.

6.2 Experimental Methodology

Documentation of the boundary layers for each set of conditions was conducted with hotwire anemom-

Figure 20: $2-D$ Thermograph of Ice Casting in Figure 4. Dark areas depict cool regions.

Figure 21: $2-D$ Thermograph of Pseudo-Random Array in Figure 18. Dark areas depict cool regions.

etry while the pressure gradient was controlled by varying the angle of attack of the plate. For each set of experimental conditions, a steady state energy balance for the plate/roughness assembly between conductive heat losses to supports, convective heat losses to the freestream, radiation heat losses, and the heat flux supplied by the IR heaters was established[2]. An IR camera then recorded the surface temperature distributions of the roughness elements using infrared thermography. The IR camera images were calibrated by the thermocouples at the plate.

6.3 Preliminary Results

The substrate was at a $-20°$ angle with respect to the $47m/s$ freestream, producing a laminar boundary layer in the favorable pressure gradient. Figure 20 shows a $2-D$ thermograph of the ice casting of Figure 4 while Figure 21 depicts the corresponding

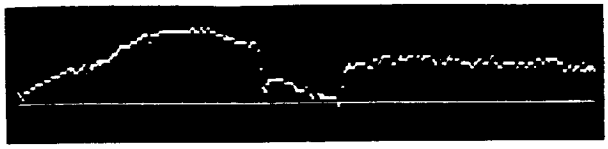

Figure 22: Temperature Distribution of Streamwise Scan Line Along Bead Row Centerline of Rectangular Roughness Array

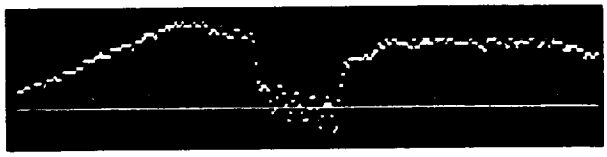

Figure 23: Temperature Distribution of Streamwise Scan Line Along Bead Row Centerline of Staggered Roughness Array

$2-D$ thermograph of the pseudo-random array in Figure 18 (flow is from left to right). The light areas represent high temperatures and therefore, low heat losses while the dark areas are cool regions where there is enhancement of heat transfer. The pseudo-random array appears to have fewer darkened areas than the casting, indicating that the surface is warmer and therefore has less enhancement of heat transfer. This is expected since the SET analysis had revealed two major bead/spacing combinations and only one (D,P) pair was used as a first approximation. Had the other (D,P) combination been used as well, more darkened areas would appear in Figure 21 and one could expect the average heat transfer coefficients of the SET-generated roughness and the casting to be in better agreement.

The temperature distribution for a $2-D$ thermograph streamwise scan line passing through the center of a row of beads on the plug in Figure 16 is shown in Figure 22. The test conditions were the same as those used for the casting and pseudo-random array. A corresponding streamwise scan line for the staggered bead array of Figure 17 is shown in Figure 23. The location of the plugs is apparent in the thermographs by the rectangular-shaped temperature drop in the center of the graph. Both roughness plugs have comparable overall temperature drops and negative temperature gradients in the streamwise direction. The temperature decrease with distance downstream may be due to the increased convective heat losses of the beads from the vorticity generated by upstream beads. Note that the effects of individual beads are apparent in the staggered bead array thermograph; there are small

temperature deficits corresponding to the location of enhanced heat transfer on the beads (Figure 23). However, no such localized temperature drops are apparent in the rectangular bead array thermograph (Figure 22). Instead, there is just a linear decrease in temperature similar to the downward trend of the staggered array thermograph. This is due to the fact that the rectangular array has a smaller effective streamwise bead spacing than the staggered array, causing an overlap of the heat transfer enhancement of the individual beads. Consequently, only the aggregate effect of the beads is apparent rather than individual contributions. This indicates that the SET model parameters have significant implications for enhancement of heat transfer. First of all, the size of the beads is clearly important for the enhancement of heat transfer. Secondly, as shown in Figures 22 and 23, the bead spacing also has an impact on heat transfer.

7 Conclusions and Future Research

SET analysis with epoxy bead deposition is a feasible method for connecting IRT images to heat transfer enhancement on surface roughness. However, since the data from the heat transfer tests are preliminary, a thorough analysis of the IR thermographs has yet to be completed. These results must then be incorporated into an improved heat transfer model for LEWICE so that predicted ice shapes can be compared to the experimentally observed ice shapes in the IRT tests. More dry heat transfer testing will be required to determine how many bead sizes from the experimental SET histograms must be retained for an accurate representation of the roughness.

In the long term, more IRT experiments are needed to develop a data set of early icing roughness over a range of cloud conditions so that more heat transfer studies can be conducted. Ideally, the SET would be applied to a direct representation of the ice surface topography rather than to uncalibrated video images. For example, the roughness data might be in the form of profilometer surveys or stereo video images. This improvement in data acquisition would eliminate much of the ambiguity inherent in ordinary video images by providing roughness height information - a key element for comparing enhanced heat transfer on real-world accretions to that observed on SET-designed roughness.

In the context of a larger aircraft icing problem, modeling the complex geometries that result from ice formation on aerodynamic surfaces is a difficult but necessary business. Understanding what types of initial roughness will arise on wings under glaze flight conditions is key to predicting how heat transfer will be enhanced on the substrate and, consequently, what global ice shapes will emerge at long time scales.

This work was supported by NASA Lewis research grant NAG 3-1761.

References

[1] G. R. Cross and A. K. Jain. Markov random field texture models. *IEEE Transactions on Pattern Analysis and Machine Intelligence*, 5(1):25–39, January 1983.

[2] R. Henry, K. S. Breuer, and R. J. Hansman Jr. Measurement of heat transfer variation on surface roughness elements using infrared techniques. *Journal of Thermophysics and Heat Transfer*, 1994.

[3] R. J. Hansman Jr., K. S. Breuer, D. Hazan, A. Reehorst, and M. Vargas. Close-up analysis of aircraft ice accretion. AIAA Paper 93-0029, January 1993.

[4] K. C. Masiulaniec, K. J. DeWitt, and N. Dukhan. Experimental technique and assessment of measuring the convective heat transfer from natural ice accretions. AIAA Paper 95-0537, January 1995.

[5] J. Nikuradse. Stromungsgesetze in rauhen rohren. *Arb. Ing.-Wes.*, 1910.

[6] D. J. Orr, K. S. Breuer, and R. J. Hansman Jr. Quantitative analysis of ice accretion roughness using spectral and stochastic techniques. AIAA Paper 95-0888, January 1995.

[7] R. W. Picard. *Texture Modeling: Temperature Effects on Markov/Gibbs Random Fields*. PhD thesis, Massachusetts Institute of Technology, 1991.

[8] K. Yamaguchi and R. J. Hansman Jr. Heat transfer on accreting ice surfaces. AIAA Paper 90-0200, January 1990.